iScience

CellPress
OPEN ACCESS

Article

Correlating structural assemblies of photosynthetic reaction centers on a gold electrode and the photocurrent - potential response

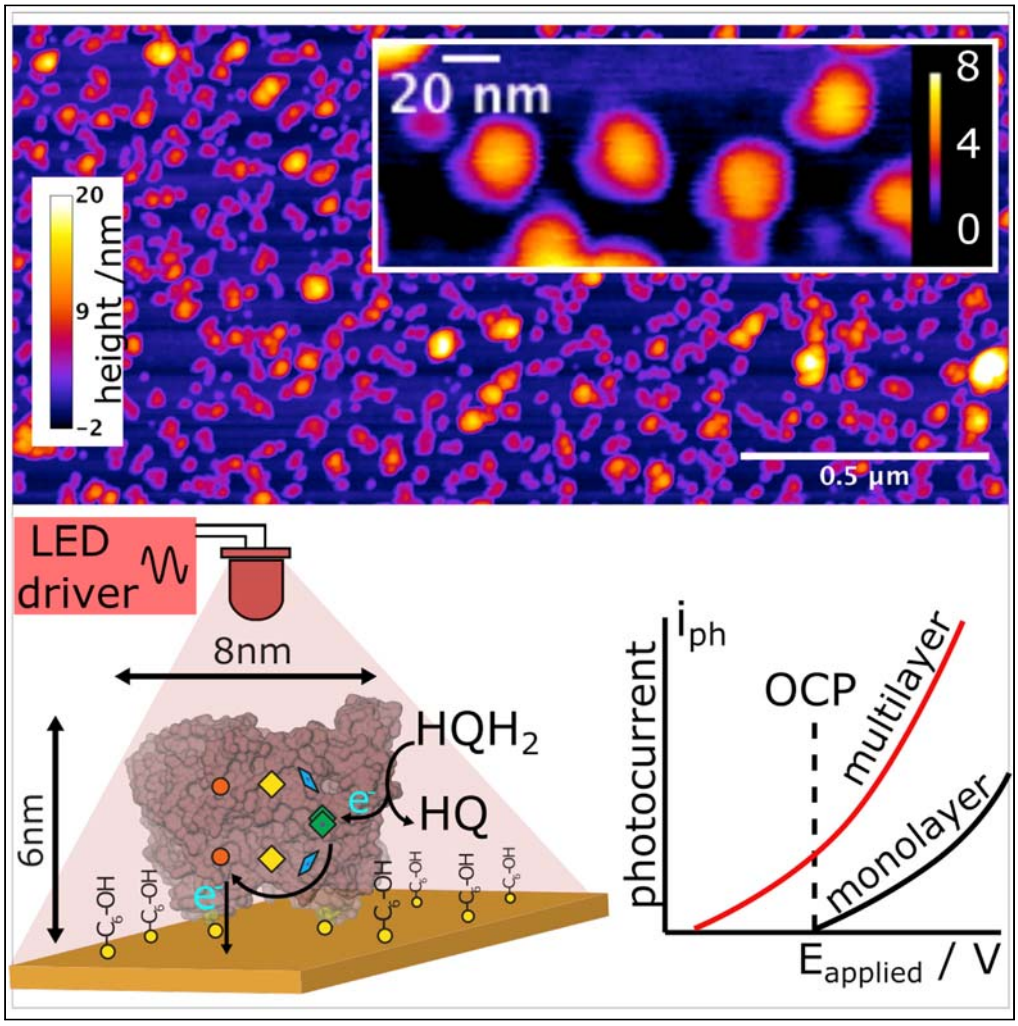

Daniel Jun, Sylvester Zhang, Adrian Jan Grzędowski, Amita Mahey, J. Thomas Beatty, Dan Bizzotto

bizzotto@chem.ubc.ca

Highlights

Controlled the formation of monolayer or multilayers of RCs on a gold electrode

Correlated electrochemical and photocurrent responses to the RC adsorbed conformations measured using AFM

Adsorbed RC conformations affect photocurrent generation

Photocurrent-potential response influenced by local redox mediator concentration and pH environment experienced by the adsorbed RCs

Jun et al., iScience 24, 102500
May 21, 2021
https://doi.org/10.1016/j.isci.2021.102500

iScience

CellPress
OPEN ACCESS

Article

Correlating structural assemblies of photosynthetic reaction centers on a gold electrode and the photocurrent - potential response

Daniel Jun,[1,3] Sylvester Zhang,[1,2] Adrian Jan Grzędowski,[1,2] Amita Mahey,[3] J. Thomas Beatty,[3] and Dan Bizzotto[1,2,4,*]

SUMMARY

The use of biomacromolecules is a nascent development in clean alternative energies. In applications of biosensors and biophotovoltaic devices, the bacterial photosynthetic reaction center (RC) is a protein-pigment complex that has been commonly interfaced with electrodes, in large part to take advantage of the long-lived and high efficiency of charge separation. We investigated assemblies of RCs on an electrode that range from monolayer to multilayers by measuring the photocurrent produced when illuminated by an intensity-modulated excitation light source. In addition, atomic force microscopy and modeling of the photocurrent with the Marcus-Hush-Chidsey theory detailed the reorganization energy for the electron transfer process, which also revealed changes in the RC local environment due to the adsorbed conformations. The local environment in which the RCs are embedded significantly influenced photocurrent generation, which has implications for electron transfer of other biomacromolecules deposited on a surface in sensor and photovoltaic applications employing a redox electrolyte.

INTRODUCTION

There has been considerable interest recently in the use of biomacromolecules for cheap, clean, and efficient sources of sustainable energy production (Ravi and Tan, 2015; Jones, 2009; Barber, 2008). One example is the modification of electrodes with biological photosynthetic protein complexes in biosensors and biophotovoltaic devices for the generation of electrical current. Photosynthetic proteins, such as reaction centers (RCs), are found in plants, algae, and photosynthetic bacteria. In particular, the RC from the bacterium *Rhodobacter sphaeroides*(Kontur et al., 2012; Mackenzie et al., 2001) has been a paradigm for the development of biohybrid solar cells due to its near perfect quantum efficiency in photon-to-electron conversion and the subsequent long-lasting quasi-stable, charge-separated state (Blankenship, 2018; Friebe and Frese, 2017; Ravi and Tan, 2015).

To date, devices incorporating RCs used a variety of methods with the aim of increasing the photocurrent, such as employing plasmonic substrates (Friebe et al., 2016a) or embedding RCs within a redox hydrogel matrix to increase surface concentration (Białek et al., 2020a). Alignment of protein complexes is possible, such as using electrostatic interactions (Mirvakili et al., 2014), gold-thiol covalent bonds (Jun et al., 2018, 2019), molecular (Trammell et al, 2004, 2006; Mahmoudzadeh et al., 2011) or protein (Yaghoubi et al., 2014; Friebe et al, 2016b, 2017; Lebedev et al., 2006) linkages, and Langmuir-Blodgett methods (Kamran et al., 2015) to deposit proteins to produce photocurrents that depended on the orientation of the complexes. However, these approaches resulted in surfaces that were likely composed of multilayers despite preparation strategies to remove non-specifically adsorbed proteins. Often, many use surfaces that are modified to prevent rather than to remove non-specifically adsorbed proteins (Campuzano et al., 2019; Siegers et al., 2004). Furthermore, there are challenges in differentiating the small photocurrents from faradaic currents when an overpotential is applied (Hollander et al., 2011). Photocurrents are typically measured at the open circuit potential (OCP), where the net faradaic current is zero for the redox system present in the electrolyte. The small photocurrents are often measured from multilayer assemblies to improve the signal to noise. We have previously established a methodology that is capable of isolating photocurrents from faradaic currents with high sensitivity enabling small photocurrents to be accurately measured even when buried in 10^4 larger faradaic currents at potentials other than the OCP (Jun et al., 2019). This method allows for fundamental studies of electron transfer energetics which require a well-defined,

[1]Advanced Materials and Process Engineering Laboratory, University of British Columbia, Vancouver, BC V6T 1Z4, Canada

[2]Department of Chemistry, University of British Columbia, Vancouver, BC V6T 1Z1, Canada

[3]Department of Microbiology and Immunology, University of British Columbia, Vancouver, BC V6T 1Z1, Canada

[4]Lead contact

*Correspondence: bizzotto@chem.ubc.ca

https://doi.org/10.1016/j.isci.2021.102500

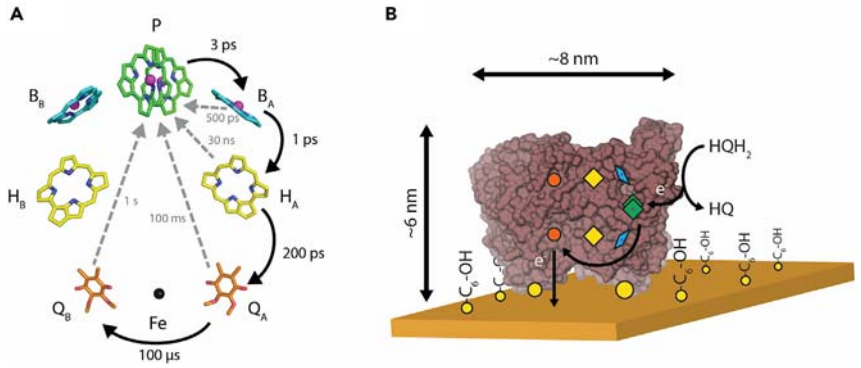

Figure 1. Schematic of the RC cofactors involved in photocurrent generation and the proposed RC configuration on the gold surface

(A) The cofactors in the RC are arranged in two symmetrical branches. The cofactors consist of the special pair bacteriochlorophylls (BChls), P (green); accessory BChls, B_A and B_B (cyan); bacteriopheophytins (BPhes), H_A and H_B (yellow); quinones, Q_A and Q_B (orange); a non-heme iron, Fe (black); and a carotenoid (not shown). The electron flow (black arrows) during charge separation is through the A-branch cofactors (denoted with a subscript A) and terminates at the Q_B quinone. The forward electron transfer and relaxation time constants are shown in black and gray respectively (Jones, 2009; Feher, 1971). Only the bacteriochlorin macrocycles and quinone headgroups are shown for simplicity. Nitrogen atoms are colored as blue, oxygen as red, magnesium as magenta, and carbon as green, cyan, yellow, or orange. The figure is based on PDB 2J8C.

(B) A schematic representation of the cysteine modified RC binding to the gold surface through a gold-thiol covalent bond (yellow circle) and the expected path of the photoexcited electrons through the RC and to the electrode surface. HQH_2 is the sacrificial reactant that reduces P^+ to P and C_6OH is 6-mercaptohexanol used to passivate the surface.

controllable surface arrangement of RCs on the electrode surface; ideally, a single monolayer of RCs adsorbed in a homogeneous manner (Gerster et al., 2012).

Assembling a uniform monolayer on an electrode surface has been accomplished for a variety of biomacromolecules, such as DNA and proteins, through self-assembly, gold-thiol covalent bonds, and displacement of non-specifically adsorbed species with a competitive agent. Here, we demonstrate that genetically modifying the RC to introduce two cysteines enables covalent binding to the gold surface (Figure 1B) and that adsorbed RCs can be arranged in different surface structure assemblies, such as a monolayer or multilayer configuration. The RC is a membrane-embedded protein-pigment complex that consists of three polypeptide chains that provide a scaffold for ten cofactors. These pigments in the RC are a dimer of bacteriochlorophyll (BChl) molecules called the "special pair" (P), two accessory BChls (B_A, B_B), two bacteriopheophytins (BPhe) (H_A, H_B), two quinones (Q_A, Q_B), a carotenoid, and an iron atom (Figure 1A). Light adsorption by P results in the excited state P*, generating an electron that cascades through B_A and H_A, reaching Q_A and forming the $P^+ Q_A^-$ charge-separated state. Electrical photocurrent flows if the RCs are oriented appropriately on an electrode for electrons to transfer from Q_A^- to the electrode (Jun et al., 2018).

The structural assemblies of electrode-bound RCs yield characteristic photocurrent-potential (i_{ph}-E) responses that can be modeled by the Marcus-Hush-Chidsey theory, and shift the potentials at which photocurrents are generated. The methodology of increasing photocurrents by increasing protein loading and measurements at the OCP may not take into consideration the underlying mechanistic processes occurring on the surface that influence electron transfer. In contrast, we are able to elucidate the differences in energetics between structural assemblies of RC monolayers or multilayers, and their effects on the relationship between photocurrent generation and the OCP.

RESULTS AND DISCUSSION

The adsorption of RC proteins onto an electrode with the goal to maximize photocurrent generation has been accomplished by deposition in thick layers (Plumeré and Nowaczyk, 2016; Ravi and Tan, 2015; Yehezkeli et al., 2014; Kamran et al., 2014; Mirvakili et al., 2014), or with RCs suspended in a redox hydrogel polymer deposited onto the electrode (Białek et al., 2020a, 2020b). Although other approaches to orient RCs have been successful in achieving large photocurrents, the possibility of significant random orientations or multilayers of RCs still remains. Large photocurrents are needed to overcome the background faradaic

currents and, consequently, these approaches make accurate energetic measurements challenging which impedes the understanding of photocurrent generation at a molecular level. Creating and measuring the photocurrents from a well-defined monomolecular assembly of RC proteins on an electrode surface are described here with this goal in mind.

The RC used in this work was engineered such that all native cysteine residues were replaced with serine or alanine residues (Dutta et al., 2014a, 2014b; Jun et al., 2018; Mahmoudzadeh et al., 2011), and through rational design, two additional cysteine residues were added on the hydrophilic regions of the RC in the vicinity of B_A and Q_A resulting in the "double mutant" RC (referred to as RC). UV-vis absorbance spectroscopy indicated no changes in the pigment cofactor absorbance bands, inferring that the protein structure was not adversely affected by the mutations (absorbance spectra provided in supplemental information). On a low-resolution millisecond timescale, the $P^+Q_A^-$ and $P^+Q_B^-$ charge recombination time constants of the RC were similar to that of previously reported values of an unmodified wild type RC (data in supplemental information) (Dutta et al., 2014b; Jun et al., 2020).

Modifying RCs with cysteine thiol moieties enables the use of gold-thiol covalent bonds for binding RCs on a gold electrode surface in a well-defined orientation. Although RCs have been bound to the P-side (Hollander et al., 2011; Kondo et al., 2007, 2012; Yaghoubi et al., 2014; Friebe et al., 2016b; Tan et al., 2012) or Q-side (Jun et al., 2018, 2019; Trammell et al., 2006) previously, our approach is different and enables binding of the RC on its side such that Q_A is closer to the electrode surface than in other configurations (Figure 1B). It is important to note that this approach will not prevent multilayer formation because RCs are large, complex protein entities and the formation of multilayers is most likely due to hydrophobic interactions and entropic energy gains. Therefore, removing multilayers and non-specifically adsorbed RCs requires a competitive adsorption strategy. For example, in thiol-based DNA self-assembled monolayers (SAMs), an approach to minimize non-specific adsorption involved an additional step where the self-assembly of small alkylthiols competitively displaced weakly interacting, non-specifically adsorbed DNA (Herne and Tarlov, 1997). Here, we used a similar strategy to prepare and characterize a monolayer of RCs on a gold electrode.

Preparing RC/MCH surfaces

The alkylthiol 6-mercaptohexanol (MCH) was used to displace multilayers and non-specifically adsorbed RCs. Additionally, MCH treatment passivated areas of the electrode not covered with RCs from the sacrificial electron donor HQH_2 and limited faradaic current. HQH_2 was used due to the favorable difference between its midpoint potential of ~250 mV vs. standard hydrogen electrode (SHE) and the P^+ reduction midpoint potential of ~500 mV vs. SHE (Jun et al., 2018, 2019; Lin et al., 1994), and has been observed to not affect or interact with the Q_B quinone pocket (Jun et al., 2018).Figure 2 shows changes in the faradaic currents from HQH_2 redox and photocurrents (i_{ph}) after RC deposition and subsequent MCH treatment. Deposition of 5 μM RCs (24 h) on bare gold resulted in HQH_2 redox behavior that was significantly reduced when compared to a clean gold surface (shown in supplemental information, Figure S1) indicating the surface was significantly blocked (Finklea et al., 1993; Diao et al., 1999). Subsequent exposure of this same surface to 100 μM MCH (1 h) decreased the faradaic current, as expected, and notably resulted in larger photocurrents. The decrease in the faradaic currents of HQH_2 redox may be due to the displacement of multilayers and non-specifically adsorbed RCs by MCH and thus better passivation of the electrode surface; an MCH SAM significantly blocked faradaic currents as shown in Figure 2A (green trace). Additionally, removing RC multilayers may allow for a larger number of photons to reach RCs that are close to the electrode surface and more efficient in electron transfer, increasing i_{ph}.

In contrast, a short deposition time of 5 μM RCs (10 min) followed by a longer incubation in 100 μM MCH (24 h) resulted in decreased photocurrent and a faradaic current that was nearly identical to that of an MCH-only surface. This indicated that an organized RC/MCH monolayer was created, resulting in a well-blocked electrode surface. The decrease in photocurrent relative to the 24 h incubation of RCs suggested that MCH displaced not only the majority of multilayers and non-specifically adsorbed RCs, but possibly also some of those covalently linked to gold, via a thiol exchange mechanism (Schlenoff et al., 1995; Baralia et al., 2005). The MCH-only surface generated a small background photocurrent signal due to the leakage of the faradaic current (~0.01%).

The removal of non-specifically adsorbed RCs and multilayers of RCs changed the i_{ph}-E response relative to an organized monolayer of RC/MCH. The i_{ph}-E relationship is addressed in subsequent sections, where we

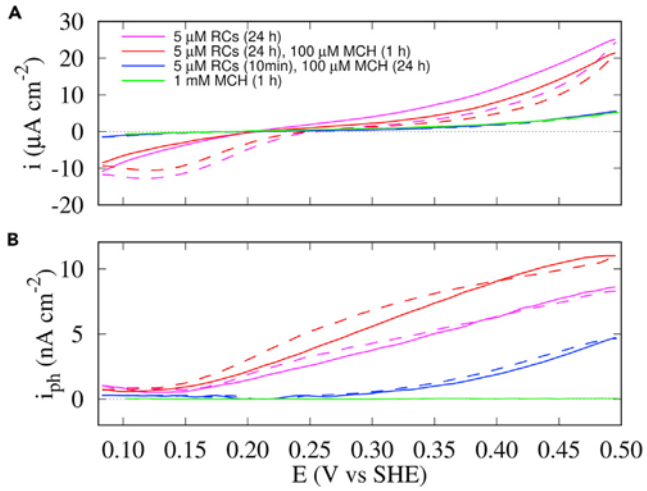

Figure 2. Faradaic currents and photocurrents measured on RC-modified gold electrodes

(A) Faradaic currents and (B) photocurrents measured from surfaces modified with deposition of RC from a 5 µM RC solution with and without MCH post treatment. An electrode surface covered with an MCH SAM is shown for comparison. Measurements were in PBS with 20 mM HQH_2, at 2 mV/s and using 810 nm LED illumination (LED characteristics provided in Table 2). (—: negative potential scan, - - -: positive potential scan).

hypothesize that organized monolayers of RC/MCH generate measurable photocurrents at an onset potential (E_{onset}) more positive than that of RC/MCH multilayers. Crucially, we have established a procedure that consistently generates RC/MCH surfaces that show the same blocking of faradaic currents as an MCH-only surface, which is essential for controlling and replicating the formation of biomolecular surfaces and redox reactions in order to make energetic measurements under well-defined conditions.

The faradaic currents shown in Figure 2A were sensitive to the changes on the surface resulting from differences in RC organization and passivation by MCH. Electrochemical impedance spectroscopy (EIS) was also measured at the OCP (+220 mV/SHE) for these surfaces. EIS provided more evidence of the change in the state of the adsorbed layers. It confirmed the increased blocking of HQH_2 redox corresponded with the increase in MCH coverage. Capacitance of the interface was also estimated though the use of a constant phase element (CPE) circuit component that also reports on the uniformity of the interfacial response to potential perturbation (details in supplemental information, Table S1). The capacitance decreased by almost 50% as the MCH content on the surface increased indicating that adsorbed RCs do not form a low dielectric layer on the electrode surface as compared to MCH, likely due to entrapped electrolyte in the disorganized layer or poor adsorption to the surface. EIS also indicated that the absence of an MCH treatment resulted in a surface that was less ordered and more heterogeneous as compared to the RC-modified surface that was treated with 100 µM MCH (24 h). This behavior was also observed for the considerably shorter 1 hr MCH treatment, which implied that significantly heterogeneous surfaces result if the electrodes are only incubated with RCs and not subsequently immersed in MCH. Additionally, EIS showed that MCH also coated the bare areas of the gold surface in addition to displacing non-specifically adsorbed or multilayers of RCs, as evidenced by the changes in capacitance and the CPE exponent. Unfortunately, EIS was unable to distinguish the characteristics of the surfaces that produced different i_{ph}-E response curves and different E_{onset} in Figure 2. This is reasonable as the comparison was based on HQH_2 redox, which is much more sensitive to the extent of surface blocking. Therefore, CV and EIS based redox measurements cannot be relied upon to detect different surface structures or explain the differences in the i_{ph}-E response curves because these techniques were neither sensitive nor specific enough. However, identification of the transition from a monolayered to a multilayered surface was revealed by the i_{ph}-E response curves.

Distinguishing a monolayer or multilayer of RCs with i_{ph}-E response curves

The photocurrents and the resulting i_{ph}-E response curves were more sensitive to the structural differences of a monolayer or multilayer configuration of RCs on the electrode surface when compared to

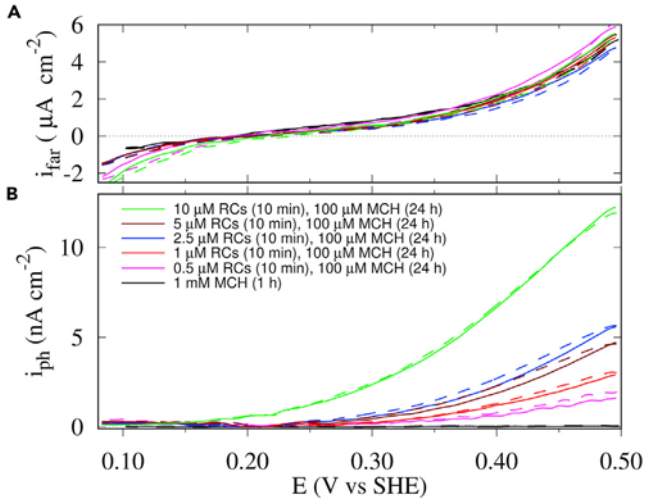

Figure 3. Faradaic currents and photocurrents measured on RC-modified gold electrodes after MCH treatment

Faradaic currents (A) and photocurrents (B) measured from gold surfaces prepared by a 10 min deposition into a solution of RC of concentrations from 0.5 µM to 10 µM, followed by post-treatment with immersion in 100 µM MCH for 24 h. An electrode surface covered with an MCH SAM is shown for comparison. Measurements were in PBS with 20 mM HQH_2, 2 mV/s sweep rate, and 810 nm LED illumination. (—: negative scan, - - -: positive scan)

electrochemical characterization. Surfaces were prepared by varying the RC concentration from 0.5 to 10 µM and maintaining the incubation time of 10 min, followed by immersion in a 100 µM MCH solution (24 hr), as previously established, to form a uniform layer of RC/MCH. The photocurrents and i_{ph}-E response curves are shown in Figure 3.

First, Figure 3 confirms that the photocurrents were not contaminated by the faradaic current of HQH_2 redox occurring concurrently because no photocurrent was measured from the MCH-only surface. Furthermore, the faradaic responses of all the RC/MCH surfaces were similar to that of an MCH coated surface, further confirming that the electrochemical response was not effective for analyzing and elucidating the structural configuration of the assembled RC adsorbates.

The i_{ph} showed similar E dependence for all the RC concentrations, with a plateau in photocurrent generation between 2.5 and 5 µM RC. A significant increase in photocurrent was observed for the surface prepared with 10 µM RC, which was also accompanied by a change in the shape of the i_{ph}-E response curve. The i_{ph}-E response showed that the onset of photocurrent increase began at a more negative potential when compared to the surfaces prepared with lower concentrations of RCs (+100 mV vs +220 mV/SHE, respectively). The potential at which the photocurrent was above the noise (>0.2 nA/cm^2) was designated as the onset potential (E_{onset}) for photocurrent generation. This negative shift in E_{onset} behavior was similar to the trend previously described with either no MCH treatment or a short time in MCH (Figure 2).

Earlier, we hypothesized that the more negative E_{onset} potential appeared to be a characteristic of RC multilayers on the electrode surface relative to a monolayer. Here, the data suggest that the transition from a monolayer to a multilayer occurs between 5 and 10 µM RC solutions. Additionally, at higher RC concentrations, despite incubation with 100 µM MCH (24 h), the negatively shifted E_{onset} value suggests the presence of multilayer features that remain on the surface after treatment.

As the other surfaces prepared with 0.5–5 µM RC showed the same E_{onset} value, we hypothesized that they consisted of a monolayer adsorbed configuration rather than a multilayer assembly on the surface. Confirmation of the hypothesis required visualization of the surface using atomic force microscopy (AFM).

AFM evaluation of the RC/MCH monolayer surface

The electrochemical and photocurrent measurements indirectly showed the differences between monolayer or multilayer structural assemblies of RCs on the electrode surface. A direct measurement using ex situ AFM confirmed the trends in the changes in the RC/MCH surface structures that resulted in the i_{ph}-

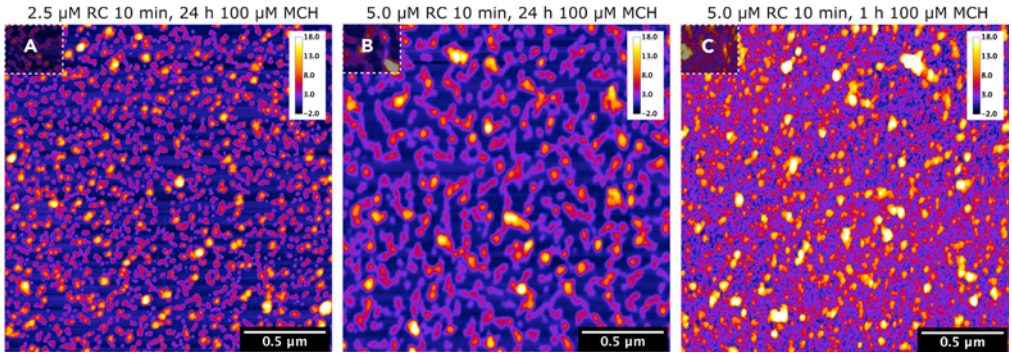

Figure 4. AFM topography of an RC-modified Au(111) facet after MCH treatment

AFM topological images from a Au(111) facet after modification with (A) 2.5 μM RC (10 min) followed by 100 μM MCH (24 h). (B) 5 μM RC (10 min), followed by 100 μM MCH (24 h), (C) 5 μM RC (10 min), followed by 100 μM MCH (1 h). The z scale represents height in nm and is the same for all figures. Topographic images using the full z scale range are provided in supplemental information. All scale bars are 500 nm.

E response curves. Surfaces were modified with RCs, as previously described, using conditions identified as representative of monolayer formation and of multilayer formation. Previously, the Au(111) facet, of a single crystal gold bead electrode was used for AFM studies as it is atomically flat (Ogaki and Itaya, 1995). In the supplemental information, Figure S2 shows a 5 × 5 μm AFM image of an MCH-coated Au(111) facet, where features of one or more atomic steps of Au (0.2 nm) are observed. These are substantially smaller than the expected height of adsorbed RCs, making this surface ideal for height determinations.

Figure 4 shows AFM images from such an Au(111) facet for three different surface preparations, clearly showing significant differences in the surface structures. Much more flat gold (set as 0 nm), which was most likely MCH covered, was visible in Figure 4A as compared to the higher coverage surfaces in Figures 4B and 4C. Essentially no MCH covered gold was observed for the high RC coverage (Figure 4C).

An estimate of the coverage and configuration of adsorbed RCs on the electrode surface was achieved using AFM imaging of the RC monolayer modified Au(111) facet. The RCs can be thought of as an elliptical cylinder that is ~8 nm in length from the P-side to the Q-side and ~5 nm in width along the elliptical minor axis; the height is ~7 nm along the elliptical major axis (Figure 1B) (Trammell et al., 2007; Jones, 2009) AFM imaging accurately measures the height of well-defined features; however, lateral dimensions are less reliable due to convolution of the tip shape with the entity being imaged. Here the tip radius and the RCs are of similar size, around 10 nm.

A 2 × 2 μm topographic AFM image of an Au(111) facet exposed to 2.5 μM RC (1 h), followed by 100 μM MCH (24 h) which is representative of monolayer formation, shown in Figure 4A. The analysis (outlined in supplemental information) of the complete 5 × 5 μm image found >8000 particles (outlined in Figure S3) that were easily identified because of the flat gold substrate that surrounded the particles. An example of the individual features observed on this surface is shown in Figure 5A along with line scans across the features and from the nearby flat Au(111) surface. Complete analysis of the maximum height distribution for all the particles found in the full 5 × 5 μm image is shown in Figure 5B (details in supplemental information'Figure S4). These particles were on average 5–7 nm high, with a broad range of heights up to 20 nm, though only ~10% were above 10 nm. The observed height corresponded well with the expected RC height of 5–7 nm, if they adsorbed to the surface as designed. The average footprint area of the 5–7 nm high particles was 350 nm^2, equivalent to a 20 nm diameter. Because tip convolution adds about 10–15 nm to the diameter, the actual diameter of these particles was closer to 6–10 nm. Given the observed heights and diameters, and known RC dimensions, most of the observed particles were single adsorbed RCs arranged in a monolayer.

Another surface was prepared, which was expected to be representative of a multilayer (5 μM RC (10 min), 100 μM MCH (1 h)), and is shown in Figure 4C (details in supplemental information, Figure S8). The surface was completely covered with particles and regions of flat gold surface were not visible, making absolute height determinations problematic. This sample was complicated to analyze, as individual isolated RCs

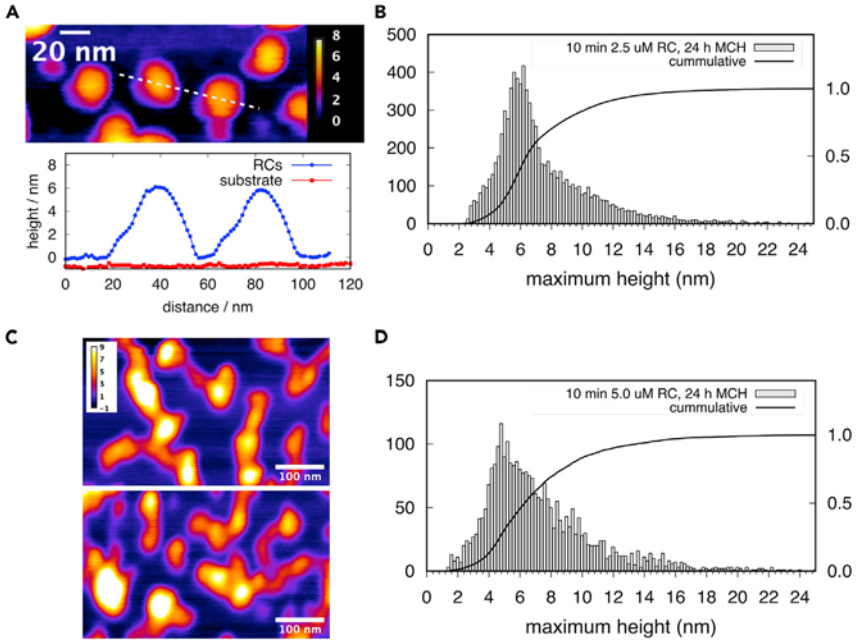

Figure 5. AFM analysis of individually adsorbed RCs on gold

Analysis of the AFM images shown in Figures 4A and 4B. (A) Zoomed-in region from the surface prepared using 2.5 μM RC (10 min) followed by 100 μM MCH (24 h) showing the individual RC particles on a flat MCH covered Au(111) surface with the corresponding height profile taken along the white dashed line. Scale bar is 20 nm.

(B) Maximum height distribution analysis for the sample in Figure 4A.

(C) Two zoomed-in regions from the 5 μM RC (10 min) followed by 100 μM MCH (24 h) showing low and medium coverage regions containing chains of RCs. Scale bar is 100 nm.

(D) Maximum height distribution from the AFM image in Figure 4B.

were not found in this multilayer configuration. Even so, the number of particles that were taller than their neighbors by 10–20 nm was significantly larger when compared to the monolayer sample (15% vs. 6% respectively).

In other experiments, a similar surface was prepared using the same solution of 5 μM RC (10 min), but followed by 100 μM MCH for 24 h, rather than 1 h. The topographic AFM image is shown in Figure 4B, and the analyses and data are shown in Figures 5C and 5D (more details in supplemental information, Figures S6 and S7). The average maximum height distribution was ~5 nm, slightly lower than the surface incubated with 2.5 μM RC, but well within the expected range. A significant fraction (>5%) of these particle heights was greater than 10 nm, suggesting the existence of multilayer formations. Interestingly, the adsorbed species were arranged differently with fewer individual isolated particles and more that appeared to be interconnected. Two different aggregation states were observed and are shown in Figure 5C. The interconnected nature may be a consequence of RC protein aggregation as a precursor to multilayer formation. Importantly, regions of bare gold were visible again that were previously obscured in the multilayer configuration.

From the i_{ph}- E response curves, the surface preparation conditions using 2.5 μM RC (10 min)followed by 100 μM MCH (24 h) and 5 μM RC (10 min) followed by 100 μM MCH (24 h) were hypothesized to generate a monolayer configuration, and a multilayer configuration for 5 μM RC (10 min) followed by 100 μM MCH (1 h). The confirmation with AFM underscores the importance of MCH treatment as necessary to remove multilayer or ill-formed adsorbate configurations. The increase in surface density of adsorbed RCs and the shift from a monolayer to a multilayer configuration corresponded to the changes observed in the photocurrent measurements, namely the shift in the E_{onset} to more negative potentials. This characteristic seems to be a signature of multilayer adsorption and becomes difficult to model due to the numerous factors that are active at the interface and in the adsorbed film (e.g., diffusion of mediator, electron transfer kinetics and thermodynamics, random or unknown orientations of the RC in the multilayer). Therefore,

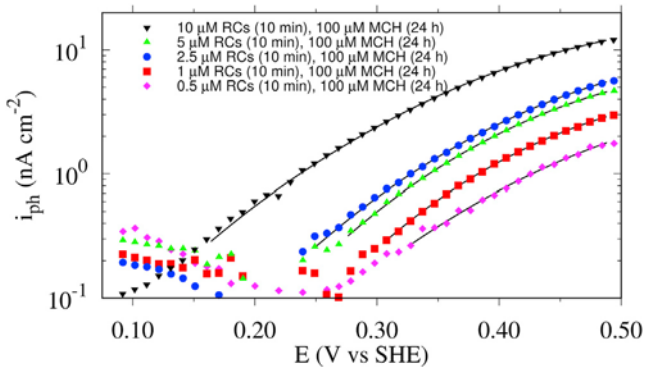

Figure 6. Marcus-Hush-Chidsey analysis of the photocurrents measured from RC-modified gold electrodes

Marcus-Hush-Chidsey fits for the i_{ph}-E curves for data shown in Figure 3 were used to fit for photocurrents >0.2 nA/cm^2. The experimental data shown are an average of the anodic and cathodic sweeps and shown as symbols (only every 25th data point) and the line represents the fit. Measurements were in PBS with 20 mM HQH_2, 2 mV/s sweep rate, and 810 nm LED illumination.

modeling of the energetics of the electron transfer event is focused on the well-defined monolayer RC/MCH surfaces.

Modeling i_{ph}-E response curves for monolayer RC/MCH surfaces

The photocurrent and AFM analysis of the RC/MCH surfaces showed that under specific deposition conditions, a well-defined monolayer of RCs can be prepared; therefore, an estimate of the electron transfer characteristics is possible. The RC is bound to the electrode surface via two cysteines, and if oriented correctly, Q_A is closest to the electrode so that electron transfer can occur. Upon absorption of a photon by P BChls, an excited state is formed, P*, and an electron rapidly cascades through a chain of cofactors to the Q_A quinone resulting in the $P^+Q_A^-$ charge-separated state. Concurrently, an HQH_2 reduces P^+ back to P. The photocurrent measured is the electron transfer from the Q_A cofactor to the electrode, driven by the difference in the potential between QA^- and the gold surface (its Fermi level). This process can be modeled by electron transfer theories, most appropriately with the Marcus-Hush-Chidsey model (Zeng et al., 2014).

The i_{ph} - E response curves of RC/MCH surfaces were fitted to the Marcus-Hush-Chidsey theory using only photocurrents greater than 0.2 nA/cm^2 (at least 5-fold larger than the smallest reliably-measured photocurrent). These RC modified surfaces were continuously illuminated with a modulation in the intensity range of 10–90% at 13 Hz, and so the photocurrents were representative of processes that were fast enough to respond to the intensity modulation. The resulting fits and parameters, such as the reorganization energy and the equilibrium potential (E_{eq}^{ph}), are given in Figure 6 and Table 1 (individual fit results shown in Figure S11). The data correlated well with theory (r^2> 0.995).

For low coverage RC monolayers prepared using 0.5 to 2.5 µM RC, the reorganization energies were on average 0.24 $\pm$ 0.03 eV and E_{eq}^{ph}= +257 $\pm$ 19 mV/SHE. The reorganization energies are similar to values reported in the literature for surface-bound RCs (Trammell et al., 2007), but smaller than for the Q_A^- to Q_B electron transfer in RCs in solution (Ptushenko and Krishtalik, 2018). Interestingly, one of the surfaces prepared with 5 µM RC showed similar results, but a repeat of this preparation had a larger reorganization energy (0.29 eV) and a more negative E_{eq}^{ph} of +217 mV/SHE (shown in supplemental information, Figure S10). Unlike lower concentrations of RCs, the 5 µM RC preparation was challenging to replicate in a monolayer and as postulated earlier, this may be the concentration at which multilayer formation and protein-protein interactions begin to exert a larger influence on adsorbed surface formation. The surface prepared with 10 µM RC also followed this trend with a reorganization energy of 0.30 eV and E_{eq}^{ph} of +152 mV/SHE. Multilayer characteristics, such as interconnected regions shown in the AFM images, are correlated to fits that yielded higher reorganization energies and more negative E_{eq}^{ph}.

The same analysis was performed on the faradaic currents measured in the same region of potential used in the photocurrent analysis. The oxidation of HQH_2 was consistent for all samples with a reorganization

Table 1. Parameters from fitting to the Marcus-Hush-Chidsey theory using only photocurrents (>0.2 nA/cm^2)

[RC] (μM)	λ_{810nm} (eV)	E_{eq}^{ph} (mV/SHE)
0.5	0.271 ±0.016	+253 ±8
1.0	0.240 ±0.001	+241 ±1
1.0	0.194 ±0.001	+286 ±1
2.5	0.248 ±0.001	+242 ±1
5.0	0.215 ±0.001	+262 ±1
5.0*	0.289 ±0.001	+217 ±1
10.0	0.301 ±0.001	+152 ±1

Uncertainties (1σ) are determined using a weighted fitting routine in MATLAB (fitnlm) with weights determined from the moving standard deviation calculated using a 20 mV window. *Large faradaic current (see data in SI: Figure S10).

energy that ranged from 0.36 to 0.44 eV with an E_{eq}^{ph} of +200 to +230 mV/SHE. All data and fits are shown in supplemental information (Table S3 and Figure S9). Fitting the photocurrents measured at the same time show distinctly different values of the reorganization energy and E_{eq}^{ph} when compared to the faradaic currents, confirming that the photocurrents measured were not influenced by the faradaic currents.

The systematic increase in the fitted reorganization energy and more negative E_{eq}^{ph} with an increase in RC coverage may indicate the presence of another RC configuration. Fitting to only one set of parameters may produce average reorganization energy and E_{eq}^{ph} resulting from two (or more) different populations of RCs on the surface or RCs in different environments. In order to elucidate the change in E_{onset} further, multilayers were evaluated using the same fitting procedure for surfaces modified with 5 μM RC (24 h) without MCH treatment as well as 5 μM RC (24 h) with 100 μM MCH (1 h) treatment.

Using a single set of parameters, the fits continued the trend observed for higher concentration RC treated surfaces, namely larger reorganization energies (0.427 eV (no MCH) and 0.247 eV (1 h MCH)) and an E_{eq}^{ph} shift to more negative potentials (−87 mV/SHE (no MCH) and +40 mV/SHE (1 h MCH)). The fit to theory improved with the addition of a second set of parameters (details in supplemental information, Tables S4 and S5 and Figure S12). One component had a reorganization energy of 0.28 ± 0.02 eV which was consistent for both multilayer samples. The E_{eq}^{ph} parameter for both samples ranged from +125 to +75 mV/SHE. This component was present at about 50% of the adsorbate for both surfaces. The second component was the same for both multilayer preparations with a small reorganization energy of 0.06 ± 0.002 eV and E_{eq}^{ph} = +150 ± 7 mV/SHE. The results from the two component fitting were consistent with one part of the surface composed of adsorbed RCs similar to a monolayer configuration and a second component, possibly distorted or denatured RCs, indicating little change in conformation during electron transfer. The same shift toward negative potentials was observed for the E_{onset} for the monolayer and multilayer samples, suggesting that E_{eq}^{ph} is closely related to or can be interpreted as E_{onset}. Although the mechanism behind the shift in E_{eq}^{ph} to negative potentials remains uncertain, we suggest a distortion of proteins that shortens the distance for electron transfer to the electrode, or changes in the local environment within the multilayers, due to restrictions in the diffusion of HQH_2, HQ, and/or H^+. This is supported by evidence of diffusion-limited currents in multilayers observed when measuring the DC photocurrent at the OCP.

DC photocurrent measurements at the OCP

To facilitate comparison with data in the literature, DC photocurrents were measured using 860 nm illumination with the potential set to the OCP (+200 to +220 mV/SHE) with three surface conditions: 5 μM RC (24 h) without MCH ("multilayer"); the same surface, but then incubated with 100 μM MCH (1 hr) ("monolayer-like"); and 2.5 μM RC (10 min), 100 μM MCH (24 h) ("monolayer"). The DC photocurrent responses are shown in the left column of Figure 7 with the right column comparing the photocurrents measured around the OCP (taken from Figure 2) using our modulated method that exclusively measures the photocurrent.

A light-dependent response was observed in which the "multilayer" surface sustained a DC photocurrent of 10 nA/cm^2 at OCP (+218 mV/SHE). This was approximately 4-fold larger than the photocurrents of 2.5 nA/cm^2 (Figure 7A ((right panel)) measured using the modulation method (i_{ph}) at +218 mV/SHE (arrow in Figure 7A(right panel)). The DC photocurrents were stable for many seconds suggesting that the current was not limited by HQH_2 reduction of P^+. Turning the light off resulted in a slow decrease in the measured

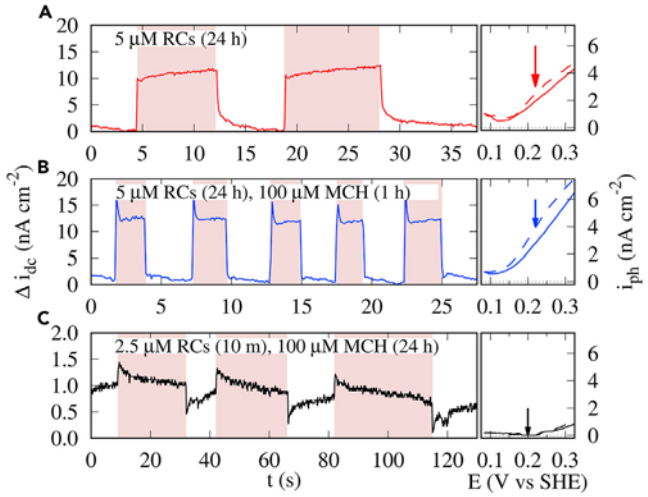

Figure 7. DC photocurrents measured from RC-modified gold electrodes

DC photocurrents measured for three samples prepared using: (A) 5 μM RC (24 h) with no MCH treatment, (B) same electrode as in (A) but with MCH (1 h) treatment, and (C) 2.5 μM RC (10 min) MCH (24 h) treatment. The photocurrents were measured at OCP (+218, +222, +203 mV/SHE for each respective surface) in PBS with 20 mM HQH_2. The red background indicates when the interface was illuminated with an 860 nm LED (characteristics in Table 2). The photocurrent shown in Figure 2 is replotted on the right panels zoomed into the region around the OCP (arrow) for the corresponding interface on the left panel.

current that lasted tens of seconds and was characterized by a diffusional response (in supplemental information, Figure S15), likely a result of the rate at which HQH_2 or HQ diffused into or out of the layer to reach equilibrium with the bulk solution. The same surface was then treated with MCH, creating a "monolayer-like" adsorbed layer, and a similar photocurrent magnitude was obtained in addition to an improved response time observed by the absence of a diffusional response. This effect was also reflected in an increase in the modulated photocurrent to 4 nA/cm^2 since the faster response would be able to produce greater photocurrents at 13 Hz (Figure 7B (right panel)). The displacement of multilayers and non-specifically adsorbed RC by MCH eliminated the diffusion behavior. Diffusion-controlled currents for RC modified electrode surfaces have been reported previously and described in multilayer models (Takshi et al., 2009; Mirvakili et al., 2014; Buesen et al., 2019). The "monolayer" surface generated a small DC photocurrent transient that rapidly returned to baseline after the light was turned on, which is in agreement with the modulated photocurrent measurement where at OCP, no i_{ph} was observed (Figure 7F). Examples of the DC photocurrents measured from other monolayer surfaces are shown in Figure S16.

Comparing photocurrent measurements for monolayer and multilayer adsorbed RCs

The DC photocurrent response of the monolayer and multilayer RC surfaces depended on the nature of the adsorbed layer; a similar dependency was observed for E_{onset} where significant i_{ph} was measured. The OCP was essentially independent of the surface configuration and similar for all the samples. The measured OCP was controlled by the HQH_2 redox species in solution (+200 to +220 mV/SHE at pH = 7.2). Classically, the OCP is the potential where the net current is zero, and reflects a balance between the rates of oxidation and reduction, dominated by the largest rates for a mixture of redox species. The use of MCH to remove non-specifically adsorbed RCs does not completely passivate the gold surface, so HQH_2 redox still takes place and controls the OCP.

The photocurrent-specific E_{onset} was shifted to more negative potentials for the multilayer compared to the monolayer RC covered surfaces. Therefore, these photocurrent measurements may be sensitive to the local environment experienced by the adsorbed RCs. For example, the difference in the E_{onset} measured from the photocurrents of the monolayer and multilayer surfaces was most likely influenced by the changes in the environment within the multilayer, which sets the local redox potential, independent of the OCP. In other words, a monolayer surface is not constrained by layers of protein that impede the access of the redox species, and therefore, the individually adsorbed RCs experience the same conditions as the

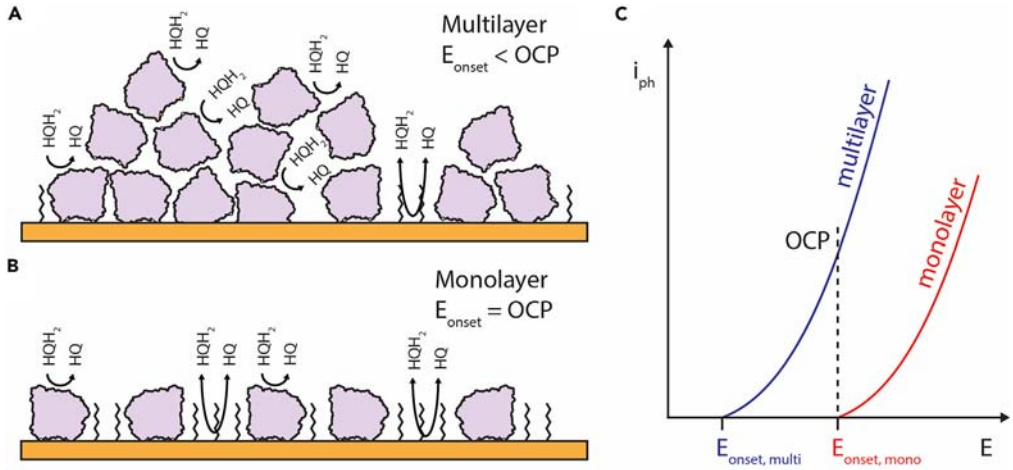

Figure 8. Schematic representation of monolayer and multilayer adsorbed RCs and their corresponding photocurrent-potential relationships

Schematic representation of the two adsorbed layers (A) multilayer and (B) monolayer on the gold surface and the HQH_2 access to the electrode surface through the MCH SAM or through the RC multilayer. (C) schematic representation of the OCP and onset potentials to the photocurrents measured.

MCH covered gold electrode surface; the opposite is the case for multilayer surfaces that may "trap" redox species and change the local redox environment.

As the E_{onset} shifted to more negative potentials, the local redox environment within the multilayer RC assembly differed from that in solution, which can be rationalized via the Nernst equation for HQH_2 redox: $E = E^{o} - \frac{0.0592}{2} log \frac{[HQH_2]}{[HQ][H^+]^2}$. The negative shift in E_{onset} would result from an increase in the $[HQH_2]/[HQ]$ ratio and/or an increase in pH within the RC multilayer. Meanwhile, the OCP measured via faradaic redox from the entire electrode would be determined by the redox conditions in the solution. Consequently, in the "multilayer" surface, the DC photocurrent measurement at OCP was performed at an overpotential of +100 mV relative to the local equilibrium potential experienced by the RCs in the adsorbed multilayer. This resulted in large photocurrent generation which also had a diffusional character when illumination was removed. Conversely, the "monolayer" surface had an E_{onset} equal to the OCP revealing that these RCs existed in a local environment in equilibrium with the solution phase. Therefore, creation of $P^+Q_A^-$ via photon absorption did not result in significant photocurrents when measured at the OCP as the measurements were performed at a negligible overpotential (Figure 8).

Confirming evidence of the influence of $[HQH_2]$ on the photocurrent and E_{onset} was obtained by measurements on a surface that had multilayer characteristics similar to the 5 μM RC sample with a short MCH treatment time (Figure S13). An increase in the $[HQH_2]$ from 5 to 30 mM correlated with increased photocurrents, a negative shift in E_{onset} (or E_{eq}^{ph} from fitting), and an increase in reorganization energy that agreed with results previously described for multilayer samples (more details in supplemental information: Figures S13 and S14 and Table S6). As expected, no significant shift in the OCP was observed for the faradaic process taking place through the MCH layer on the electrode surface. Therefore, the negative shift in E_{onset} was correlated to the increase in $[HQH_2]$. Partitioning of HQH_2 into the RC multilayer would increase the local concentration of HQH_2, consequently shifting the E_{onset} for photocurrents to more negative potentials, and explaining the difference between the E_{onset}values for multilayer and monolayer surfaces.

Figure 8 shows a schematic of the multilayer and monolayer samples detailing the local environment and its relationship to the measured photocurrents. The photocurrent measurements are sensitive to the adsorbed states of the RCs and their interfacial environment. This reveals that the DC photocurrent measurements done at the OCP provide a limited evaluation of the surface modifications. Moreover, manipulation of the local redox environment could influence the driving force (overpotential) that controls the magnitude of the generated photocurrents. These factors result in an uncertainty of the measurement of electron transfer energetics that are important for understanding the activity of the adsorbed RC and the electron

transfer to an electrode from an adsorbed RC protein. Finally, the influence of the redox conditions in local interfacial regions plays an important role for surfaces modified with molecular adsorbates emphasizing the need for approaches that can distinguish between cases where the conditions of the interface and the bulk solution differ.

Conclusions

The conditions for preparing a gold surface covered with a monolayer of RC covalently tethered via thiol bonds was determined with a modulated illumination intensity method that measured the photocurrent-potential response in addition to ex situ AFM. The photocurrent response under an applied potential for an electrode surface with a partial to full monolayer of adsorbed RCs was fitted to the Marcus-Hush-Chidsey theoretical formalism and a consistent reorganization energy of 0.24 $\pm$ 0.03 eV was determined with an equilibrium potential (E_{eq}^{ph}) of +257 $\pm$ 19 mV/SHE. The photocurrent characteristics were sensitive enough to reveal the initiation of multilayer formation on the gold electrode. Multilayer coated electrode surfaces showed a significant negative shift in the photocurrent E_{onset} and a photocurrent-potential response that was best fit using two components, one with the same reorganization energy as the monolayer samples, and the other component having a close to zero reorganization energy (<0.1 eV). AFM imaging confirmed the presence of isolated adsorbed RCs with 7 nm heights for the monolayer covered surfaces. AFM also showed multilayer formation as aggregated adsorbed species and tall structures. The negative shift in the E_{onset} for multilayers of RCs was hypothesized to be a result of the difference in the local redox conditions present within the adsorbed multilayer. The difference between the local redox potential and the OCP, defined by the redox couple in solution, may create conditions for large DC photocurrents.

Limitations of the study

The formation of RC monolayers requires proteins that are not significantly oxidized or aggregated. The use of freshly prepared proteins is ideal, but aggregation occurs over time resulting in some reproducibility challenges in making monolayer RC surfaces. The method for measuring the photocurrents can distinguish between monolayer and multilayer samples. The photocurrent signals are very small, which requires a high performance lock-in-amplifier that is capable of working at frequencies below 20 Hz, and not all amplifiers will be able to measure these signals reliably.

STAR★METHODS

Detailed methods are provided in the online version of this paper and include the following:

- KEY RESOURCES TABLE
- RESOURCE AVAILABILITY
  - Lead contact
  - Materials availability
  - Data and code availability
- METHOD DETAILS
  - Protein purification
  - Materials
  - Deposition of RCs
  - Faradaic and photocurrent measurements
  - DC photocurrent measurement
  - Electrochemical impedance spectroscopy (EIS)
  - AFM
- QUANTIFICATION AND STATISTICAL ANALYSIS
  - Photocurrent analysis
  - EIS data analysis

SUPPLEMENTAL INFORMATION

Supplemental information can be found online at https://doi.org/10.1016/j.isci.2021.102500.

ACKNOWLEDGMENTS

This research was supported by grants from the Natural Sciences and Engineering Research Council of Canada (NSERC) to D.B. (RGPIN 2016-05528) and J.T.B. (RGPIN 2018-03898). SZ was funded by anNSERC USRA.

AUTHOR CONTRIBUTIONS

Conceptualization, D.J. and D.B.; Methodology, D.J. and D.B.; Investigation, S.Z., A.G. and D.J.; Writing – Original Draft, D.J., S.Z. and D.B.; Writing – Review & Editing, D.J., J.T.B and D.B.; Funding Acquisition, J.T.B and D.B.; Resources, D.B., D.J., A.M., and J.T.B.; Supervision, D.J., J.T.B., and D.B.

DECLARATION OF INTERESTS

The authors declare no competing interests.

INCLUSION AND DIVERSITY

One or more of the authors of this paper self-identifies as an underrepresented ethnic minority in science.

Received: January 27, 2021
Revised: March 22, 2021
Accepted: April 28, 2021
Published: May 21, 2021

REFERENCES

Baralia, G.G., Duwez, A.S., Nysten, B., and Jonas, A.M. (2005). Kinetics of exchange of alkanethiol monolayers self-assembled on polycrystalline gold. Langmuir *21*, 6825–6829. https://doi.org/10.1021/la050245v.

Barber, J. (2008). Photosynthetic energy conversion: natural and artificial. Chem. Soc. Rev. *38*, 185–196. https://doi.org/10.1039/b802262n.

Białek, R., Friebe, V., Ruff, A., Jones, M.R., Frese, R., and Gibasiewicz, K. (2020a). In situ spectroelectrochemical investigation of a biophotoelectrode based on photoreaction centers embedded in a redox hydrogel. Electrochim.Acta *330*, 135190. https://doi.org/10.1016/j.electacta.2019.135190.

Białek, R., Thakur, K., Ruff, A., Jones, M.R., Schuhmann, W., Ramanan, C., and Gibasiewicz, K. (2020b). Insight into electron transfer from a redox polymer to a photoactive protein. J. Phys. Chem. B *124*, 11123–11132. https://doi.org/10.1021/acs.jpcb.0c08714.

Blankenship, R.E. (2018). In Molecular Mechanisms of Photosynthesis, 1st Edition (Blackwell Science Ltd), p. 35.

Buesen, D., Hoefer, T., Zhang, H., and Plumeré, N. (2019). A kinetic model for redox-active film based biophotoelectrodes. Faraday Discuss. *215*, 39–53. https://doi.org/10.1039/c8fd00168e.

Campuzano, S., Pedrero, M., Yáñez-Sedeño, P., and Pingarrón, J.M. (2019). Antifouling (Bio) materials for electrochemical (Bio)sensing. Int. J. Mol. Sci. *20*, 423. https://doi.org/10.3390/ijms20020423.

Diao, P., Jiang, D., Cui, X., Gu, D., and Tong, R. (1999). Studies of structural disorder of self-assembled thiol monolayers on gold by cyclic voltammetry and ac impedance. J. Electroanal. Chem. *464*, 61–67. https://doi.org/10.1016/S0022-0728(98)00470-7.

Dutta, P.K., Levenberg, S., Loskutov, A., Jun, D., Saer, R., Beatty, J.T., Lin, S., Liu, Y., Woodbury, N.W., and Yan, H. (2014a). A DNA-directed light-harvesting/reaction center system. J. Am. Chem. Soc. *136*, 16618–16625. https://doi.org/10.1021/ja509018g.

Dutta, P.K., Lin, S., Loskutov, A., Levenberg, S., Jun, D., Saer, R., Beatty, J.T., Liu, Y., Yan, H., and Woodbury, N.W. (2014b). Reengineering the optical absorption cross-section of photosynthetic reaction centers. J. Am. Chem. Soc. *136*, 4599–4604. https://doi.org/10.1021/ja411843k.

Feher, G. (1971). Some chemical and physical properties of a bacterial reaction center particle and its primary photochemical reactants. Photochem.Photobiol. *14*, 373–387.

Finklea, H.O., Snider, D.A., Fedyk, J., Sabatani, E., Gafni, Y., and Rubinstein, I. (1993). Characterization of Octadecanethiol-Coated Gold electrode as microarray electrodes by cyclic voltammetry and ac impedance spectroscopy. Langmuir *9*, 3660–3667. https://doi.org/10.1021/la00036a050.

Friebe, V.M., Delgado, J.D., Swainsbury, D.J.K., Gruber, J.M., Chanaewa, A., Grondelle, R.v., Hauff, E.v., Millo, D., Jones, M.R., and Frese, R.N. (2016a). Plasmon-enhanced photocurrent of photosynthetic pigment proteins on nanoporous silver. Adv. Funct.Mater. *26*, 285–292. https://doi.org/10.1002/adfm.201504020.

Friebe, V.M., and Frese, R.N. (2017). Photosynthetic reaction center-based biophotovoltaics. Curr.Opin.Electrochem. *5*, 126–134. https://doi.org/10.1016/j.coelec.2017.08.001.

Friebe, V.M., Millo, D., Swainsbury, D.J.K., Jones, M.R., and Frese, R.N. (2017). Cytochrome c provides an electron-funneling antenna for efficient photocurrent generation in a reaction center biophotocathode. ACS Appl. Mater. Interfaces *9*, 23379–23388. https://doi.org/10.1021/acsami.7b03278.

Friebe, V.M., Swainsbury, D.J.K., Fyfe, P.K., Heijden, W.V.D., Jones, M.R., and Frese, R.N. (2016b). On the mechanism of ubiquinone mediated photocurrent generation by a reaction center based photocathode. Biochim.Biophys. Acta *1857*, 1925–1934. https://doi.org/10.1016/j.bbabio.2016.09.011.

Gerster, D., Reichert, J., Bi, H., Barth, J.V., Kaniber, S.M., Holleitner, A.W., Visoly-Fisher, I., Sergani, S., and Carmeli, I. (2012). Photocurrent of a single photosynthetic protein. Nat. Nano *7*, 673–676. https://doi.org/10.1038/nnano.2012.165.

Herne, T.M., and Tarlov, M.J. (1997). Characterization of DNA probes immobilized on gold surfaces. J. Am. Chem. Soc. *119*, 8916–8920.

Hollander, M.J.d., Magis, J.G., Fuchsenberger, P., Aartsma, T.J., Jones, M.R., and Frese, R.N. (2011). Enhanced photocurrent generation by photosynthetic bacterial reaction centers through molecular relays, light-harvesting complexes, and direct protein–gold interactions. Langmuir *27*, 10282–10294. https://doi.org/10.1021/la2013528.

Jones, M.R. (2009). The petite purple photosynthetic powerpack. Biochem. Soc. Trans. *37*, 400–407. https://doi.org/10.1042/bst0370400.

Jun, D., Beatty, J.T., and Bizzotto, D. (2019). Highly sensitive method to isolate photocurrent signals from large background redox currents on protein-modified electrodes. ChemElectroChem *6*, 2870–2875. https://doi.org/10.1002/celc.201900249.

Jun, D., Dhupar, H.S., Mahmoudzadeh, A., Duong, F., Madden, J.D.W., and Beatty, J.T.

(2018). In vivo assembly of a truncated H subunit mutant of the Rhodobacter sphaeroides photosynthetic reaction centre and direct electron transfer from the QAquinone to an electrode. Photosynth. Res. *137*, 227–239. https://doi.org/10.1007/s11120-018-0493-0.

Jun, D., Richardson-Sanchez, T., Mahey, A., Murphy, M.E.P., Fernandez, R.C., and Beatty, J.T. (2020). Introduction of the menaquinone biosynthetic pathway into rhodobacter sphaeroides and de novo synthesis of menaquinone for incorporation into heterologously expressed integral membrane proteins. ACS Synth. Biol. *9*, 1190–1200. https://doi.org/10.1021/acssynbio.0c00066.

Jun, D., Saer, R.G., Madden, J.D., and Beatty, J.T. (2014). Use of new strains of Rhodobacter sphaeroides and a modified simple culture medium to increase yield and facilitate purification of the reaction centre. Photosynth. Res. *120*, 197–205. https://doi.org/10.1007/s11120-013-9866-6.

Kamran, M., Delgado, J.D., Friebe, V., Aartsma, T.J., and Frese, R.N. (2014). Photosynthetic protein complexes as bio-photovoltaic building blocks retaining a highinternal quantum efficiency. Biomacromolecules *15*, 2833–2838. https://doi.org/10.1021/bm500585s.

Kamran, M., Friebe, V.M., Delgado, J.D., Aartsma, T.J., Frese, R.N., and Jones, M.R. (2015). Demonstration of asymmetric electron conduction in pseudosymmetrical photosynthetic reaction centre proteins in an electrical circuit. Nat. Commun. *6*, 6530. https://doi.org/10.1038/ncomms7530.

Kondo, M., Iida, K., Dewa, T., Tanaka, H., Ogawa, T., Nagashima, S., Nagashima, K.V.P., Shimada, K., Hashimoto, H., Gardiner, A.T., et al. (2012). Photocurrent and electronic activities of oriented-His-tagged photosynthetic light-harvesting/reaction center core complexes assembled onto a gold electrode. Biomacromolecules *13*, 432–438. https://doi.org/10.1021/bm201457s.

Kondo, M., Nakamura, Y., Fujii, K., Nagata, M., Suemori, Y., Dewa, T., Iida, K., Gardiner, A.T., Cogdell, R.J., and Nango, M. (2007). Self-assembled monolayer of light-harvesting core complexes from photosynthetic bacteria on a gold electrode modified with alkanethiols. Biomacromolecules *8*, 2457–2463. https://doi.org/10.1021/bm070352z.

Kontur, W.S., Schackwitz, W.S., Ivanova, N., Martin, J., LaButti, K., Deshpande, S., Tice, H.N., Pennacchio, C., Sodergren, E., Weinstock, G.M., et al. (2012). Revised sequence and annotation of the rhodobacter sphaeroides 2.4.1 genome. J. Bacteriol. *194*, 7016–7017. https://doi.org/10.1128/jb.01214-12.

Lasia, A. (2014). Electrochemical Impedance Spectroscopy and its Applications (Springer). https://doi.org/10.1007/978-1-4614-8933-7.

Lebedev, N., Trammell, S.A., Spano, A., Lukashev, E., Griva, I., and Schnur, J. (2006). Conductive wiring of immobilized photosynthetic reaction center to electrode by cytochrome c. JACS *128*, 12044–12045. https://doi.org/10.1021/ja063367y.

Lin, X., Murchison, H.A., Nagarajan, V., Parson, W.W., Allen, J.P., and Williams, J.C. (1994). Specific alteration of the oxidation potential of the electron donor in reaction centers from Rhodobacter sphaeroides. Proc. Natl. Acad. Sci. USA *91*, 10265–10269. https://doi.org/10.1073/pnas.91.22.10265.

Mackenzie, C., Choudhary, M., Larimer, F.W., Predki, P.F., Stilwagen, S., Armitage, J.P., Barber, R.D., Donohue, T.J., Hosler, J.P., Newman, J.E., et al. (2001). The home stretch, a first analysis of the nearly completed genome of Rhodobacter sphaeroides 2.4.1. Photosynth. Res. *70*, 19–41. https://doi.org/10.1023/a:1013831823701.

Mahmoudzadeh, A., Saer, R., Jun, D., Mirvakili, S.M., Takshi, A., Iranpour, B., Ouellet, E., Lagally, E.T., Madden, J.D.W., and Beatty, J.T. (2011). Photocurrent generation by direct electron transfer using photosynthetic reaction centres. Smart Mater.Struct. *20*. https://doi.org/10.1088/0964-1726/20/9/094019.

Mirvakili, S.M., Slota, J.E., Usgaocar, A.R., Mahmoudzadeh, A., Jun, D., Mirvakili, M.N., Beatty, J.T., and Madden, J.D.W. (2014). Photoactive electrodes incorporating Electrosprayed bacterial reaction centers. Adv. Funct.Mater. *24*, 4789–4794. https://doi.org/10.1002/adfm.201400350.

Nečas, D., and Klapetek, P. (2012). Gwyddion: an open-source software for SPM data analysis. Cent. Eur. J. Phys. *10*, 181–188. https://doi.org/10.2478/s11534-011-0096-2.

Ogaki, K., and Itaya, K. (1995). In situ scanning tunneling microscopy of underpotential and bulk deposition of silver on gold (111). Electrochim. Acta *40*, 1249–1257. https://doi.org/10.1016/0013-4686(95)99706-2.

Plumeré, N., and Nowaczyk, M.M. (2016). Biophotoelectrochemistry of photosynthetic proteins. In Biophotoelectrochemistry: From Bioelectrochemistry to Biophotovoltaics, L.J.C. Jeuken, ed. (Springer International Publishing), pp. 111–136. https://doi.org/10.1007/10_2016_7.

Ptushenko, V.V., and Krishtalik, L.I. (2018). Reorganization energies of the electron transfer reactions involving quinones in the reaction center of Rhodobacter sphaeroides. Photosynth. Res. *138*, 167–175. https://doi.org/10.1007/s11120-018-0560-6.

Ravi, S.K., and Tan, S.C. (2015). Progress and perspectives in exploiting photosynthetic biomolecules for solar energy harnessing. Energ Environ.Sci. *8*, 2551–2573. https://doi.org/10.1039/c5ee01361e.

Schindelin, J., Arganda-Carreras, I., Frise, E., Kaynig, V., Longair, M., Pietzsch, T., Preibisch, S., Rueden, C., Saalfeld, S., Schmid, B., et al. (2012). Fiji: an open-source platform for biological-image analysis. Nat. Methods *9*, 676–682. https://doi.org/10.1038/nmeth.2019.

Schlenoff, J.B., Li, M., and Ly, H. (1995). Stability and self-exchange in alkanethiol monolayers. J. Am. Chem. Soc. *117*, 12528–12536. https://doi.org/10.1021/ja00155a016.

Siegers, C., Biesalski, M., and Haag, R. (2004). Self-assembled monolayers of dendritic polyglycerol derivatives on gold that resist the adsorption of proteins. Chem. Eur. J. *10*, 2831–2838. https://doi.org/10.1002/chem.200306073.

Takshi, A., Madden, J.D., and Beatty, J.T. (2009). Diffusion model for charge transfer from a photosynthetic reaction center to an electrode in a photovoltaic device. Electrochim. Acta *54*, 3806–3811. https://doi.org/10.1016/j.electacta.2009.01.084.

Tan, S.C., Crouch, L.I., Mahajan, S., Jones, M.R., and Welland, M.E. (2012). Increasing the open-circuit voltage of photoprotein-based photoelectrochemical cells by manipulation of the vacuum potential of the electrolytes. ACS Nano *6*, 9103–9109. https://doi.org/10.1021/nn303333e.

Trammell, S.A., Griva, I., Spano, A., Tsoi, S., Tender, L.M., Schnur, J., and Lebedev, N. (2007). Effects of distance and driving force on photoinduced electron transfer between photosynthetic reaction centers and gold electrodes. J. Phys. Chem. C *111*, 17122–17130. https://doi.org/10.1021/jp0740402.

Trammell, S.A., Spano, A., Price, R., and Lebedev, N. (2006). Effect of protein orientation on electron transfer between photosynthetic reaction centers and carbon electrodes. Biosens.Bioelectron. *21*, 1023–1028. https://doi.org/10.1016/j.bios.2005.03.015.

Trammell, S.A., Wang, L., Zullo, J.M., Shashidhar, R., and Lebedev, N. (2004). Orientated binding of photosynthetic reaction centers on gold using Ni-NTA self-assembled monolayers. Biosens.Bioelectron. *19*, 1649–1655. https://doi.org/10.1016/j.bios.2003.12.034.

Yaghoubi, H., Li, Z., Jun, D., Lafalce, E., Jiang, X., Schlaf, R., Beatty, J.T., and Takshi, A. (2014). Hybrid wiring of the Rhodobacter sphaeroides reaction center for applications in bio-photoelectrochemical solar cells. J. Phys. Chem. C *118*, 23509–23518. https://doi.org/10.1021/jp507065u.

Yehezkeli, O., Tel-Vered, R., Michaeli, D., Willner, I., and Nechushtai, R. (2014). Photosynthetic reaction center-functionalized electrodes for photo-bioelectrochemical cells. Photosynth. Res. *120*, 71–85. https://doi.org/10.1007/s11120-013-9796-3.

Zeng, Y., Smith, R.B., Bai, P., and Bazant, M.Z. (2014). Simple formula for Marcus–Hush–Chidsey kinetics. J. Electroanal. Chem. *735*, 77–83. https://doi.org/10.1016/j.jelechem.2014.09.038.

STAR★METHODS

KEY RESOURCES TABLE

REAGENT or RESOURCE	SOURCE	IDENTIFIER
Software and algorithms		
ImageJ or FUJI	ver 2.1.0/1.53c	https://imagej.net/Fiji
Gwyddion	ver 2.55	http://gwyddion.net
Matlab	R2020a	
Nova	ver 1.11	https://metrohm-autolab.com
Other		
SRS 830	Stanford Research Systems	https://www.thinksrs.com
Metrohm PGStat 30	Metrohm Autolab	https://metrohm-autolab.com
AFM Agilent 5500	Keysight Technologies	https://www.keysight.com

RESOURCE AVAILABILITY

Lead contact

Further information and requests for resources and reagents should be directed to and will be fulfilled by the lead contact, Dan Bizzotto (bizzotto@chem.ubc.ca)

Materials availability

There are restrictions to the availability of the DM RC due to the viability of supply and long-term storage. The *Rhodobacter sphaeroides* strain containing the plasmid expressing the DM RC may be available upon request.

Data and code availability

This study did not generate datasets.

METHOD DETAILS

Protein purification

The previously published cysteine-less RC (Mahmoudzadeh et al., 2011), where all native cysteines were substituted with serine or alanine, was used as starting material to make genetic modifications. Two cysteine residues were introduced (A51C on the H subunit, W59C on the L subunit), yielding the "double mutant" (DM) RC and to enable chemisorption onto a gold electrode surface.

Purification of the DM RCs followed a previously published protocol of using a His-tag and affinity chromatography (Jun et al., 2014). RCs were stored at a concentration of 5 or 10 μM in PBS pH 7.2 (1.8 mM KH_2PO_4, 10 mM Na_2HPO_4, 2.7 mM KCl, 137 mM NaCl)and with 0.03% lauryldimethylamine oxide (LDAO) detergent. The absorption spectrum and RC stability data are given in the SI.

Materials

Gold flag electrodes were prepared from gold sheets. The electrodes were electrochemically cleaned by cyclic voltammetry (CV) in 100 mM KOH (25 mV/s), for 15 cycles then flame annealed in a butane flame. This was repeated until a consistent CV was measured with a clean double layer region. Estimates of the real surface area were obtained by capacitance and using gold oxide reduction charge measurements. All currents reported are normalized to the real surface area of the gold electrodes, not the geometric area. Ultrapure type I water (18.2 MΩ cm) from a Milli-Q Integral 5 system was used for all solutions. A stock solution of 1 M hydroquinone (HQH_2, 99% Sigma-Aldrich) was prepared in dimethyl sulfoxide (DMSO, Sigma-Aldrich) and diluted into PBS as required. Working solutions of 6-mercaptohexanol (MCH, 99% Sigma-Aldrich) were prepared biweekly from a stock of 50 mM MCH in HPLC-grade methanol and then diluted in PBS.

Table 2. LED characteristics

Peak emission λ_p	Half-width $\Delta\lambda$ (nm)	Half intensity beam angle (deg)	Datasheet power consumption
810 nm	40	7	20 mW
860 nm	30	3	70 mW

Deposition of RCs

Gold flag electrodes were immersed in a PBS solution of RCs (100 μL in a 1.5 mL microcentrifuge tube), as described previously (Jun et al., 2019). Electrodes were then removed from the RC solution and immersed in PBS to remove excess RCs. Subsequently, surfaces were immersed in a freshly prepared solution of 100 μM MCH in PBS as required.

Faradaic and photocurrent measurements

Electrochemical measurements were performed in PBS with an Ag/AgCl reference electrode (EDAQ ET072-1), and a platinum counter electrode. The electrolyte was not deaerated. All potentials were converted to standard hydrogen electrode (SHE). The PBS buffer contained 20 mM HQH_2. This sacrificial reactant was required to regenerate the RC (reduce P^+) which resulted in large faradaic current at potentials away from the OCP. The photocurrents were measured at applied potentials between -0.4 V/SHE and +0.1 V/SHE using a light intensity modulated method in the presence of a large faradaic background current as described previously (Jun et al., 2019). Briefly, both sides of the gold flag electrode were illuminated using the output from two LEDs (810 nm, DigiKey Part #1125-1158-ND), one on each side. The LEDs were connected to an LED driver (ILX Lightwave) which applied a constant current (40 mA) to which was added a 13 Hz 30 mA sine wave resulting in a peak-peak amplitude of 70 mA with a DC offset of 40 mA. The LED characteristics are given in Table 2. A potentiostat (Metrohm PGStat30) and scan generator (PAR175) were used to scan the potential of the gold electrode at 2 mV/s starting at OCP, and going between +0.1 V/SHE and -0.4 V/SHE for two cycles ensuring repeatable measurements (~15 min). The total electrochemical current was measured and the same current signal was analyzed with a lock-in amplifier (SRS830) which measured the amplitude and phase of the embedded 13 Hz photocurrent signal.

DC photocurrent measurement

The DC photocurrent was measured at the OCP by using the 865 nm LED (Digikey Part#475-1200-ND). The OCP was first measured until it stabilized (<3 min). This potential was then applied, and after ensuring only a very small faradaic current (<0.1 μA), the DC photocurrent measurements were made. The electrochemical current was continuously measured while turning on and off the LED. The difference in current was taken as the photocurrent. Illumination was turned off after a maximum of 10 s, and the interface was allowed to equilibrate for 10 s. This procedure was repeated multiple times. Small changes in the background current (< 10 nA) when the LED was turned off were baseline corrected.

Electrochemical impedance spectroscopy (EIS)

EIS was measured in the presence of HQH_2 at the OCP using 5 mV RMS perturbation over a narrow frequency range (10 Hz to 3 kHz) with the high frequency limit due to the RE characteristics. Two equivalent circuits were used for fitting the impedance depending on the extent of faradaic reaction measured. Impedance spectra were fit to an equivalent circuit composed of a solution resistance (R_{soln}) in series with a parallel combination of a constant phase element (Q) and a resistor representing the charge transfer resistance for the redox reaction (R_{ct}). The results from the fitting were not normalized to the area of the working electrode (5.5 cm^2). A CPE was used to model the electrode interface, and an estimate of capacitance was calculated using a previously published procedure (Lasia, 2014).

AFM

AFM images were obtained using an Agilent/Keysight 5500 microscope, operating in tapping mode in air. A single crystal gold bead electrode was used that presented large flat (111) facets enabling imaging at sub nm height resolution (see supplemental information for an example of an AFM of the MCH coated electrode surface). The bead electrode was modified with RCs, was rinsed with PBS then water and dried under argon. The (111) feature was aligned by laser reflection. The electrode was transferred into the AFM and the (111) feature was found under an optical microscope mounted in the AFM. Standard rectangular silicon

nitride tips purchased from BudgetSensors with aluminum reflective coating were used. The resonance frequency was measured to be 121 kHz, with a spring constant of 5 N/m. The tip was scanned over 8 μm at 0.14 lines/s, with one image consisting of 4,096 lines. Gwyddion (Nečas and Klapetek, 2012) and ImageJ or FUJI (Schindelin et al., 2012) were used to analyze the images. Before further detailed analysis, the AFM results were treated in Gwyiddion by flattening using polynomial background correction, aligning rows, and correcting for scars if needed. The modified images were analyzed using Fuji. They were zeroed to the bare gold surface, or to the minimum height measured. A threshold of 1 nm was set and a mask created. The mask was eroded twice and dilated once. The resulting image was segmented via watershed transformation to delineate or separate the particles. The mask was used to analyze the AFM image restricting the particles to be >3 pixels in area and excluded any particles on the edge of the image. A histogram of the maximum height for each particle was created, as well as the distribution of the footprint area of each particle.

QUANTIFICATION AND STATISTICAL ANALYSIS

Photocurrent analysis

Fitting to Marcus-Hush-Chidsey was performed using Matlab function fitnlm on the average of the positive and negative scan measured at 2 mV/s. The photocurrent was smoothed (Gaussian-weighted moving average) over a 5 mV window and the experimental error was estimated by calculating the standard deviation using a moving 20 mV window over these smoothed data. The standard deviation was used as a weighting parameter in the non-linear fits to the approximation of the Marcus-Hush-Chidsey theory provided by Zeng et al. (2014). The error in the fitted parameters reported in the tables is the standard error of the estimate.

Two component fits were also performed in the same manner with a partial F-test used to verify statistical significance of the additional component. Performing an F-test which compares the reduced model (one component, 3 parameters) against the full model (two components, 6 parameters) will calculate a F statistic. If this calculated value is larger than that in a table of F scores at the appropriate significance level ($\alpha = 0.05$, 95%), it indicates that the improvement in the fitting of the data by adding an extra component is statistically significant. This depends on the degrees of freedom for both models. The F value can be calculated using:

$$F = \frac{(SSE_{reduced} - SSE_{full})/(\text{change in the number of parameters})}{MSE_{full}}$$

where SSE is the sum of squared errors and $MSE = \frac{SSE_{full}}{n-k}$ where n = number of observations (~900) and k is the number of independent variables for the full (2 component) model (=6). For example, in the 5 μM RC (24 h) 100 μM MCH (0 h) sample, $F = \frac{(400-8)/(6-3)}{0.0092} = 1.4 \times 10^4$. The F statistic for 95% with two degrees of freedom (1 for each model) is 161. Therefore, the fit using the two component model is statistically better. This is based on the same approach outlined in Lasia, 2014.

EIS data analysis

The NOVA software controlling the Metrohm Autolab potentiostats was used to fit to the equivalent circuits. The errors reported are the standard deviations reported by the fitting program. Data above 3 kHz were not used in the fitting as the reference electrode introduced significant distortions in the impedance of the complete electrochemical cell.